



Article

# Hydrogen-Bonding Assembly of Coordination Polymers Showing Reversible Dynamic Solid-State Structural Transformations

Hitoshi Kumagai <sup>1,†</sup>, Sadahiro Yagishita <sup>2,3</sup>, Ken Kanazashi <sup>2,3</sup>, Mariko Ishii <sup>2</sup>, Shinya Hayami <sup>4,5</sup>, Hisashi Konaka <sup>6</sup>, Ryuta Ishikawa <sup>2,\*</sup>  and Satoshi Kawata <sup>2,\*</sup>

<sup>1</sup> Institute for Molecular Science, Nishigounaka 38, Myoudaiji, Okazaki 444-8585, Japan; kumagai@mosk.tytlabs.co.jp

<sup>2</sup> Department of Chemistry, Faculty of Science, Fukuoka University, 8-19-1 Nanakuma, Jonan-ku, Fukuoka 814-0180, Japan; yagishita-s@zr.dkkk.co.jp (S.Y.); kanazashi-ken@zr.dkkk.co.jp (K.K.); ic.fu.maishi@gmail.com (M.I.)

<sup>3</sup> Daiichi Kigenso Kagaku Kogyo Co., Ltd., 1-6-38 Hirabayashi-minami, Suminoe-ku, Osaka 559-0025, Japan

<sup>4</sup> Department of Chemistry, Faculty of Advanced Science and Technology, Kumamoto University, 2-39-1 Kurokami, Chuo-ku, Kumamoto 860-8555, Japan; hayami@kumamoto-u.ac.jp

<sup>5</sup> Institute of Pulsed Power Science, Kumamoto University, Kumamoto University, 2-39-1 Kurokami, Chuo-ku, Kumamoto 860-8555, Japan

<sup>6</sup> XRD Application & Software Development, X-ray Instrument Division, Rigaku Corporation, 3-9-12 Matsubara, Akishima, Tokyo 196-8666, Japan; konaka@rigaku.co.jp

\* Correspondence: ryutaishikawa@fukuoka-u.ac.jp (R.I.); kawata@fukuoka-u.ac.jp (S.K.)

† Present address: Toyota Central R and D Labs. Inc., 41-1 Yokomichi, Nagakute, Aichi 480-1192, Japan.

Received: 24 September 2018; Accepted: 18 October 2018; Published: 21 October 2018



**Abstract:** We herein report the synthesis, single-crystal structures of coordination polymers, and structural transformations of complexes employing 1,4,5,6-tetrahydro-5,6-dioxo-2,3-pyrazinedicarbonitrile (tdpd<sup>2-</sup>) and pyrazine (pyz) as bridging ligands. {[M(H<sub>2</sub>O)<sub>4</sub>(pyz)][M(tdpd)<sub>2</sub>(pyz)]·6(H<sub>2</sub>O)}<sub>n</sub>, [1·10H<sub>2</sub>O and 2·10H<sub>2</sub>O where M = Co (1) and Zn (2)], consists of two types of crystallographically independent one-dimensional (1D) structures packed together. One motif, [M(tdpd)<sub>2</sub>(pyz)]<sup>2-</sup> (A), is an anionic infinite pyz bridged 1D array with chelating tdpd<sup>2-</sup> ligands, and the other motif is a cationic chain, [M(H<sub>2</sub>O)<sub>4</sub>(pyz)]<sup>2+</sup> (B), which is decorated with four terminal water molecules. The 1D arrays (A) and (B) are arranged in parallel by multi-point hydrogen-bonding interactions in an alternate (A)(B)(A)(B) sequence extending along the *c*-axis. Both compounds exhibit structural transformations driven by thermal dehydration processes around 350 K to give partially dehydrated forms, 1·2H<sub>2</sub>O and 2·2H<sub>2</sub>O. The structural determination of the partially dehydrated form, 2·2H<sub>2</sub>O, reveals a solid-state structural transformation from a 1D chain structure to a two-dimensional (2D) coordination sheet structure, [Zn<sub>2</sub>(tdpd)<sub>2</sub>(H<sub>2</sub>O)<sub>2</sub>(pyz)]<sub>n</sub> (2·2H<sub>2</sub>O). Further heating to 500 K yields the anhydrous form 2. While the virgin samples of 1·10H<sub>2</sub>O and 2·10H<sub>2</sub>O crystallize in different crystal systems, powder X-ray diffraction (PXRD) measurements of the dehydrated forms, 1·2H<sub>2</sub>O and 2·2H<sub>2</sub>O, are indicative of the same structure. The structural transformation is irreversible for 1·10H<sub>2</sub>O at ambient conditions. On the other hand, compound 2·10H<sub>2</sub>O shows a reversible structural change. The solid-state structural transformation for 1·10H<sub>2</sub>O was also confirmed by monitoring in-situ magnetic susceptibility, which is consistent with other thermally-induced measurements.

**Keywords:** cobalt; zinc; pyrazine; coordination polymer; metal–organic framework; 1D array; solid-state structural transformation

## 1. Introduction

Coordination polymers containing guest molecules are very attractive research subjects due to their flexibilities and tunable functional applications, which provide an opportunity to develop advanced functional materials [1–5]. To design coordination polymers with excellent performance, the synergistic effects between the metal ions, ligands, and guest molecules are essential factors [6–9]. Weak but significant supramolecular interactions between coordination frameworks and guest molecules, as well as reversible metal–ligand covalent bonds which generate notable flexibility of structural topologies and enhance functionalities, are quite important in supramolecular compounds [10].

Flexible frameworks with bistable phases exhibit solid-state structural transformations involving the rearrangement of bonds driven by external stimuli such as heat, light, and pressure [11–17]. Structural transformations are generally accompanied by removal or exchange of coordinated and/or uncoordinated solvents or guests, changes in coordination number of metal ions, and conformational changes in ligands. Such structural transformations sometimes cause specific sorption behavior related to a breathing effect [1,2,6,18,19]. However, reports on the effects in bistable and flexible assemblies are limited, especially in supramolecular frameworks generated from low-dimensional assemblies or discrete molecules. Generally, such structural changes in response to external stimuli are facilitated by weak bonding interactions. These structural transformations induced by chemical and/or physical processes are much more complicated than those encountered in rigid frameworks. Therefore, investigations of solid-state structural transformations between bistable phases in flexible frameworks, such as HOFs (hydrogen-bonded organic frameworks) [20,21] and correlation with their properties, are crucial to design smart, functional materials.

The  $\text{tdpd}^{2-}$  ( $\text{H}_2\text{tdpd}$  = 1,4,5,6-tetrahydro-5,6-dioxo-2,3-pyrazinedicarbonitrile) anion attracted our interest as a potential bifunctional ligand with hydrogen-bonding characteristics. This dianion has both multiple metal-binding and multiple hydrogen bonding sites. Previously, we established that the use of anions containing two AAA sets from  $[\text{M}(\text{tdpd})_2(\text{H}_2\text{O})_2]^{2-}$  together with melaminium cations containing one DDD set (A = hydrogen bond acceptor, D = hydrogen bond donor) [22,23] leads to the formation of complementary, triply hydrogen bonded modules in the solid state, even when the products are crystallized from a competitive solvent such as water. In all cases, the building module is further extended by additional hydrogen-bonding interactions to produce tapes, and tapes are then assembled into sheets. We have also reported (II) ion/ $\text{tdpd}^{2-}$ /exo-bidentate ligands such as pyz and 4,4'-bipyridine (4,4'-bpy) [24]. The pyz and 4,4'-bpy molecules have been utilized as bridging ligands to form two-dimensional (2D) metal–organic frameworks. In this contribution, we extend the chemistry of the metal– $\text{tdpd}$  assembly by capitalizing on the competitive and facilitative hydrogen and/or coordination bonding interactions in the assemblies. We aim to control the structural transformations triggered by sorption of coordinated and interstitial solvents. In addition to the crystal structures, sorption and thermal properties are also described.

## 2. Results and Discussion

### 2.1. X-Ray Structures

#### 2.1.1. Structures of $1 \cdot 10\text{H}_2\text{O}$ and $2 \cdot 10\text{H}_2\text{O}$

The crystallographic data appear in Table 1, and selections of the relevant bond distances and angles are given in Table 2. The crystals belong to the triclinic system,  $P-1$ ,  $a = 7.0728(9)$  Å,  $b = 10.3625(13)$  Å,  $c = 12.0604(16)$  Å,  $\alpha = 67.284(4)^\circ$ ,  $\beta = 81.212(4)^\circ$ ,  $\gamma = 77.056(4)^\circ$ ,  $V = 792.48(18)$  Å<sup>3</sup>,  $Z = 1$  for  $1 \cdot 10\text{H}_2\text{O}$ , and the monoclinic system,  $P2_1/n$ ,  $a = 12.0699(3)$  Å,  $b = 7.11859(17)$  Å,  $c = 18.4918(5)$  Å,  $\beta = 98.7958(9)^\circ$ ,  $V = 1570.14(7)$  Å<sup>3</sup>,  $Z = 2$  for  $2 \cdot 10\text{H}_2\text{O}$ . While the crystal systems are different from each other, structural determinations of the two compounds revealed that the two

compounds are similar. Thus, we describe the structure of 1·10H<sub>2</sub>O, and then mention the difference between 1·10H<sub>2</sub>O and 2·10H<sub>2</sub>O.

**Table 1.** Crystallographic data for 1·10H<sub>2</sub>O, 2·10H<sub>2</sub>O and 2·2H<sub>2</sub>O.

Compound	1·10H <sub>2</sub> O	2·10H <sub>2</sub> O	2·2H <sub>2</sub> O
Formula	C <sub>20</sub> H <sub>28</sub> Co <sub>2</sub> N <sub>12</sub> O <sub>14</sub>	C <sub>20</sub> H <sub>28</sub> Zn <sub>2</sub> N <sub>12</sub> O <sub>14</sub>	C <sub>20</sub> H <sub>12</sub> Zn <sub>2</sub> N <sub>12</sub> O <sub>6</sub>
Crystal system	Triclinic	Monoclinic	Monoclinic
Space group	<i>P</i> -1	<i>P</i> 2/ <i>n</i>	<i>C</i> 2/ <i>m</i>
<i>a</i> /Å	7.0728(9)	12.0699(3)	21.0743(11)
<i>b</i> /Å	10.3625(13)	7.11859(17)	7.1528(3)
<i>c</i> /Å	12.0604(16)	18.4918(5)	8.0963(5)
<i>α</i> /°	67.284(4)	90	90
<i>β</i> /°	81.212(4)	98.7958(9)	98.773(2)
<i>γ</i> /°	77.056(4)	90	90
<i>V</i> /Å <sup>3</sup>	792.48(18)	1570.14(7)	1206.17(11)
<i>Z</i>	1	2	2
<i>R</i> 1 <sup>1</sup>	0.0977	0.0213	0.0766
<i>wR</i> 2 <sup>1</sup>	0.1893	0.0583	0.1014
<i>S</i> (GOF) <sup>1</sup>	1.109	1.131	1.5331

<sup>1</sup> Definitions:  $R1 = \sum ||F_o| - |F_c|| / \sum |F_o|$ ,  $wR2 = [\sum(w(|F_o|^2 - |F_c|^2)^2) / \sum w(F_o^2)^2]^{1/2}$  and  $S = \sum[w(|F_o|^2 - |F_c|^2)^2 / (n - p)]^{1/2}$ , where *n* is the number of reflections and *p* is the total number of parameters refined.

**Table 2.** Selected bond distances (Å) and angles (°) for 1·10H<sub>2</sub>O, 2·10H<sub>2</sub>O and 2·2H<sub>2</sub>O.

Compound	1·10H <sub>2</sub> O		2·10H <sub>2</sub> O		2·2H <sub>2</sub> O	
	(A)	(B)	(A)	(B)		
M–N	2.102(5)	2.096(5)	2.1781(15)	2.1668(15)	2.149(8)	
			2.1652(15)	2.1599(15)	2.161(7)	
M–O	2.080(3)	2.059(4)	2.0878(9)	2.0888(9)	2.186(7)	2.340(6)
	2.092(3)	2.094(4)	2.0862(9)	2.0996(9)	1.964(3)	1.961(11)
N–M–N	180.0	180.0	180.0	180.0	180.0	180.0
O–M–N	88.89(19)	90.6(2)	90.35(2)	92.11(3)	90.0(2)	
	91.11(19)	89.4(2)	89.65(2)	87.89(3)	90.00(17)	
	87.3(2)	89.9(2)	89.27(2)	87.54(3)		
	92.7(2)	90.1(2)	90.73(2)	92.46(2)		
O–M–O	180.0	91.42(15)	80.58(3)	86.98(4)	80.8(2)	89.0(4)
	100.11 (13)	88.58(15)	99.43(3)	93.20(4)	99.2(3)	180.0

Single-crystal structure analysis of 1·10H<sub>2</sub>O shows that the crystal structure of 1·10H<sub>2</sub>O consists of two crystallographically-independent and distinct polymeric structures packed together with interstitial water molecules. Figure 1 shows the crystal structure of 1·10H<sub>2</sub>O. Both of the polymeric structures consist of chains of octahedral cobalt (II) ions bridged by pyzs and interstitial waters. The key feature of the structure is the presence of two types of charged one-dimensional (1D) chains and lattice water molecules within the crystal. One of the motifs with the composition of [Co(tdpd)<sub>2</sub>(pyz)]<sup>2−</sup> (A) is an anionic infinite pyz bridged 1D array that is decorated with two chelating tdpd<sup>2−</sup> ligands. The other motif with the composition of [Co(H<sub>2</sub>O)<sub>4</sub>(pyz)]<sup>2+</sup> (B) is a cationic infinite pyz bridged 1D array that is decorated with four terminal water molecules. In total, 1·10H<sub>2</sub>O can be formulated as {[A(B)]·6(H<sub>2</sub>O)}<sub>n</sub>, and the oxidation states of all independent cobalt centers in the chain are +2. In the 1D array (A), the Co(1) center lies on a crystallographic special position, and displays a six-coordinate elongated octahedral geometry, consisting of two nitrogen atoms of pyz in the *trans* position, and four oxygen atoms of chelating tdpd<sup>2−</sup> ligands in the basal plane. The octahedrons are distorted with O–Co(1)–O bond angles [79.89(13)°] and the Co(1)–N bond distances [2.102(5) Å] are longer than the Co–O bond distances [2.080(3) and 2.092(3) Å], thus the elongation axis is N–Co–N, which runs in the chain direction. The bond angle of N–Co(1)–N [180.0°] is linear, thus Co(1)–pyz–Co(1) sequences make a straight chain. The Co···Co distance within 1D array (A) is 7.07 Å with Co–pyz–Co connectivity.

In the 1D array (B), the Co(2) center also lies on a crystallographic special position and displays a six-coordinate distorted  $\{CoN_2O_4\}$  octahedral geometry, consisting of two nitrogen atoms of pyz in the *trans* position, and four oxygen atoms of coordinated water molecules. The water molecules form the basal plane. Co(2)–N bond distances are 2.096(5) Å, and Co(2)–O bond distances are 2.094(5) and 2.059(4) Å. The N–Co(2)–N bond angle  $[180.0^\circ]$  is similar to that of the 1D array (A), and indicates a linear chain structure of the 1D array (B). The Co $\cdots$ Co distance of 7.07 Å within the 1D array (B) is similar to that found in the 1D array (A) with Co–pyz–Co connectivity. While the bond distances of Co(2) are similar to those found in Co(1), the O–Co(2)–O bond angles are larger (ranging from  $88.58(15)^\circ$ – $91.42(15)^\circ$ ) than those found in 1D array (A). This is due to the chelating  $tdpd^{2-}$  ligand found in the 1D array (A).

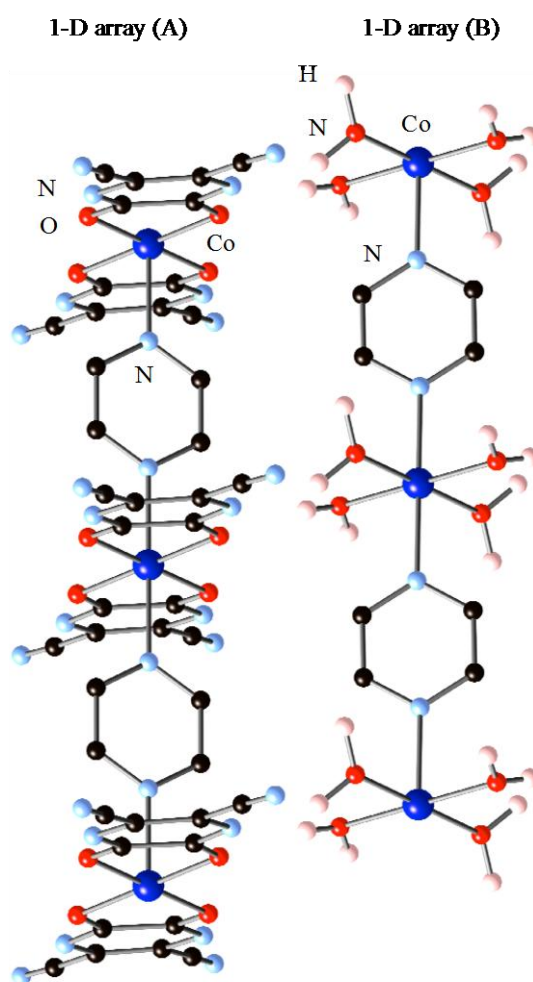


**Figure 1.** Structures of 1D arrays,  $[Co(tdpd)_2(pyz)]^{2-}$  (A) and  $[Co(H_2O)_4(pyz)]^{2+}$  (B).

Figure 2 shows the hydrogen-bonding interactions between the 1D arrays (A) and (B) and the water molecules. The 1D arrays (A) and (B) are involved in an AA–DD (A = hydrogen-bond acceptor, D = hydrogen-bond donor) arrangement. The nearest neighbor inter-chain Co $\cdots$ Co distance is 6.03 Å. Four coordinated water molecules of 1D array (B) act as hydrogen-bonding donors and the chelating  $tdpd^{2-}$  ligand acts as a hydrogen-bonding acceptor. The coordinated water molecules of 1D array (B) strongly interact with an oxygen atom and a nitrogen atom of 1D array (A) with an O–H $\cdots$ O distance of 2.673(5) Å and an OH $\cdots$ N distance of 2.789(7) Å. The inter-chain hydrogen-bond distances are very similar to that of a 1D chain compound in which a structural transformation from a 1D chain into a 3D framework was observed [25]. The basal planes of 1D arrays (A) and (B) are arranged in parallel by multi-point hydrogen-bonding interactions in an alternate (A)(B)(A)(B) sequence extending along

the *c*-axis. There are six uncoordinated water molecules, which act not only as hydrogen-bond donors to 1D array (A), but also as hydrogen-bond acceptors to 1D array (B), with the distances of 2.75(3) and 2.648(17) Å, respectively. The overall structure is formed by octahedral cobalt(II) ions,  $\text{CoN}_2\text{O}_4$ , which are connected to one another by bridging pyz ligands, a chelating  $\text{tdpd}^{2-}$  ligand, and water molecules to give a 2D hydrogen-bonding network structure.

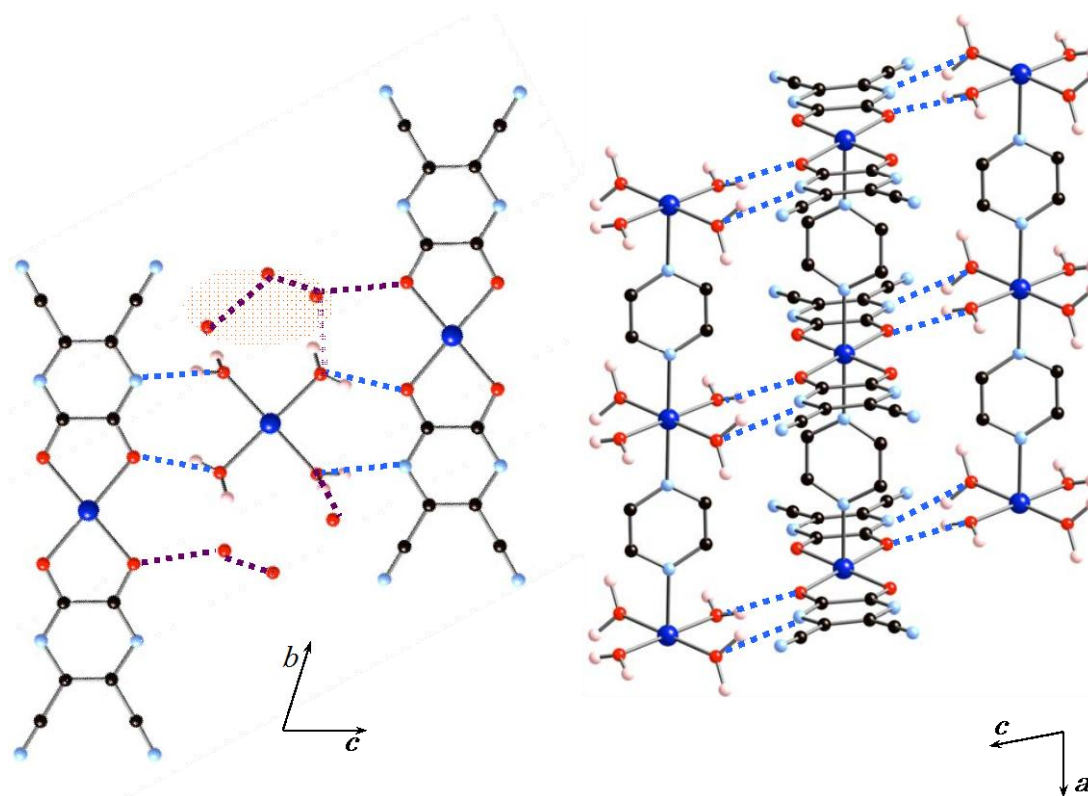


**Figure 2.** Hydrogen-bonding interactions between the 1D arrays (A) and (B) and the water molecules. Dashed lines indicate hydrogen-bonding interactions.

Different from  $1 \cdot 10\text{H}_2\text{O}$ ,  $2 \cdot 10\text{H}_2\text{O}$  crystallizes in the monoclinic system, space group  $P2_1/n$ . While the crystal system and the space group are different, X-ray crystal structure analyses of  $1 \cdot 10\text{H}_2\text{O}$  and  $2 \cdot 10\text{H}_2\text{O}$  revealed that the complexes have similar asymmetric units, metal ions,  $\text{tdpd}^{2-}$  ligands, pyz bridging ligands, and water molecules. The coordination environment of the Zn(II) ion and the binding modes of the  $\text{tdpd}^{2-}$  ligand, pyz bridging ligand, and water molecules are similar to those found in  $1 \cdot 10\text{H}_2\text{O}$ . The major difference in both compounds is the N–M(II)–O bond angles and N–M(II)–O–C torsion angles in 1D array (A). While the N–Co–O bond angle and N–Co–O–C torsion angle are  $88.90^\circ$  and  $100.4^\circ$ , respectively, the N–Zn–O bond angle and N–Zn–O–C torsion angle are  $90.35^\circ$  and  $88.72^\circ$ , respectively. Thus, the  $\text{tdpd}^{2-}$  ligands are tilted in the 1D array (A) in  $1 \cdot 10\text{H}_2\text{O}$ , however, they are nearly perpendicular to the 1D array (A) in  $2 \cdot 10\text{H}_2\text{O}$ .

### 2.1.2. Structure of $2 \cdot 2\text{H}_2\text{O}$

The crystal belonged to the monoclinic system,  $C2/m$ ,  $a = 21.0743(11)$  Å,  $b = 7.1528(3)$  Å,  $c = 8.0963(5)$  Å,  $\beta = 98.7773(2)^\circ$ ,  $V = 1206.17(11)$  Å<sup>3</sup>,  $Z = 2$  for  $2 \cdot 2\text{H}_2\text{O}$  (Figure S1 and Tables 1 and 2). X-ray structure analysis of  $2 \cdot 2\text{H}_2\text{O}$  revealed the formation of a 2D sheet structure. Figure 3 shows the 2D sheet structure of  $2 \cdot 2\text{H}_2\text{O}$ . The sheet consists of anionic 1D arrays of  $[\text{Zn}(\text{tdpd})_2(\text{pyz})]^{2-}$  (A) and cationic 1D arrays of  $[\text{Zn}(\text{H}_2\text{O})_2(\text{pyz})]^{2+}$  (B'), in which two coordinated water molecules are lost from 1D array (B). 1D arrays (A) and (B') are inter-connected by coordination bonding between oxygen atoms of  $\text{tdpd}^{2-}$  ligands and zinc(II) ions of 1D array (B') to give a neutral sheet structure.

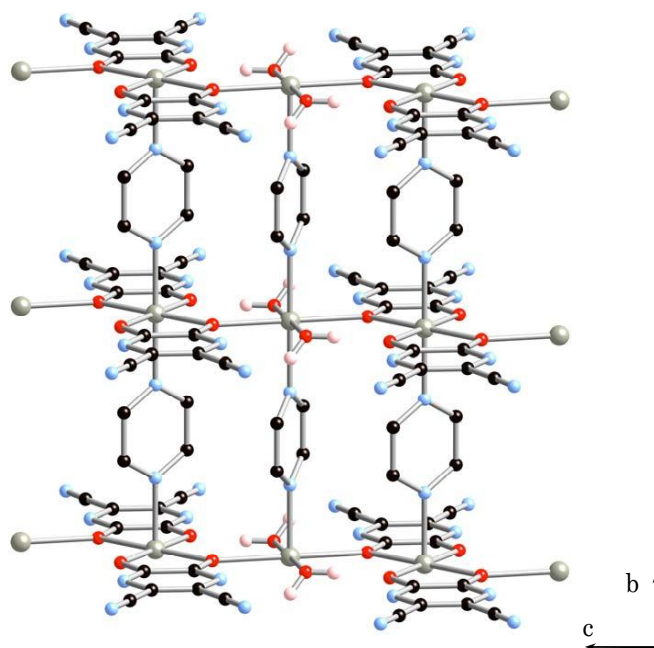


Figure 3. 2D sheet structure of  $2 \cdot 2\text{H}_2\text{O}$ .

## 2.2. TGA and PXRD Measurements

To assess the thermal and structural stability as a function of temperature, thermogravimetric analysis (TGA) and temperature-dependent powder X-ray diffraction (PXRD) patterns were measured on single-phase polycrystalline samples for  $1 \cdot 10\text{H}_2\text{O}$  and  $2 \cdot 10\text{H}_2\text{O}$ . TG curves of  $1 \cdot 10\text{H}_2\text{O}$  and  $2 \cdot 10\text{H}_2\text{O}$  are shown in Figure 4. Both compounds exhibit similar TG traces, characterized by two weight loss steps in the range of 300–550 K at a heating rate of 5 K/min. The first weight loss of 82% from 300 K to 350 K corresponds to the loss of eight molecules of water to give partially dehydrated forms,  $1 \cdot 2\text{H}_2\text{O}$  and  $2 \cdot 2\text{H}_2\text{O}$ , and the second weight loss at 450 K of 10% is due to the loss of two water molecules to give the anhydrous phase, compounds 1 and 2. Both compounds exhibit rapid weight losses from room temperature and plateaus in the TG diagrams between the first and second weight loss steps. Plateaus in the TG diagrams are indicative of thermal stabilities of the partially dehydrated forms,  $1 \cdot 2\text{H}_2\text{O}$  and  $2 \cdot 2\text{H}_2\text{O}$ .

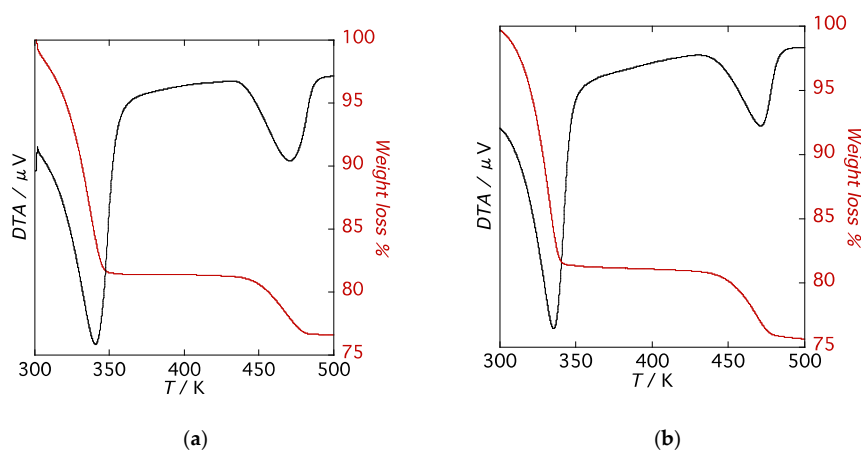
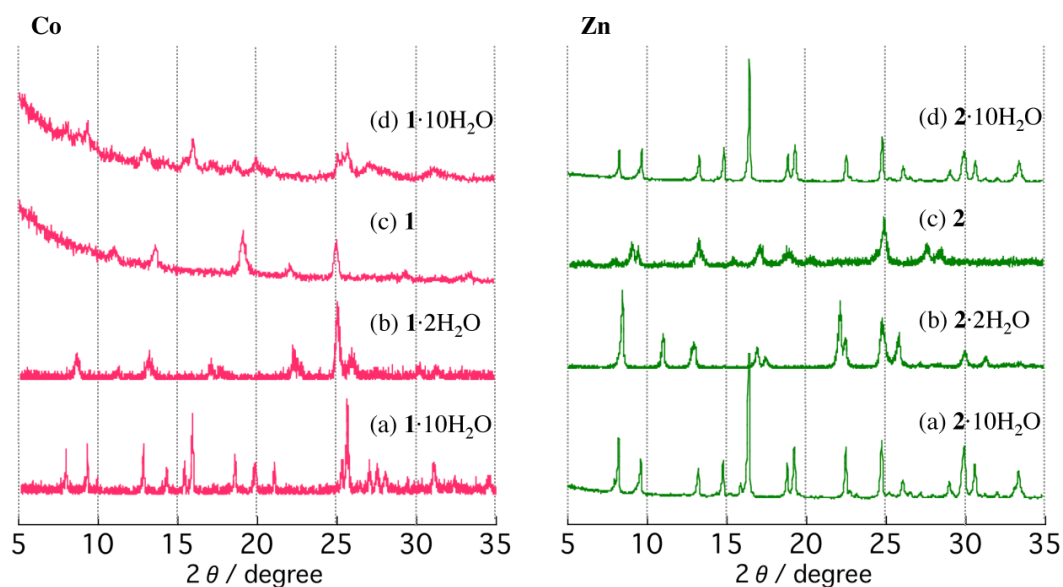


Figure 4. TG curves of (a)  $1 \cdot 10\text{H}_2\text{O}$  and (b)  $2 \cdot 10\text{H}_2\text{O}$ .

Since the single-crystals of (a)  $1 \cdot 10\text{H}_2\text{O}$  and (b)  $2 \cdot 10\text{H}_2\text{O}$  do not survive the dehydration process, the temperature-dependent PXRD patterns were measured up to 550 K in air to monitor the structural changes (Figure 5). Both crystalline powders of (a)  $1 \cdot 10\text{H}_2\text{O}$  and (b)  $2 \cdot 10\text{H}_2\text{O}$  were heated to 350 K,

the temperature at which the first weight loss steps were finished to form a partially dehydrated form. The PXRD patterns of the virgin samples at room temperature match well with the simulated patterns based on the single-crystal structures. The partially dehydrated forms of the compounds at 350 K exhibit different diffraction peaks from those of the virgin samples. The results are indicative of structural transformations driven by thermal dehydration processes. We note that the virgin samples of  $1 \cdot 10\text{H}_2\text{O}$  and  $2 \cdot 10\text{H}_2\text{O}$  crystallize in different crystal systems to give different diffraction patterns. However, the partially dehydrated forms,  $1 \cdot 2\text{H}_2\text{O}$  and  $2 \cdot 2\text{H}_2\text{O}$ , show similar PXRD patterns, suggesting that the partially dehydrated structures of  $1 \cdot 2\text{H}_2\text{O}$  and  $2 \cdot 2\text{H}_2\text{O}$  are very similar. The PXRD patterns of the partially dehydrated forms,  $1 \cdot 2\text{H}_2\text{O}$  and  $2 \cdot 2\text{H}_2\text{O}$ , indicate that the structures are not globally changed up to 450 K. Line broadening, changes in intensities, and slight shifts of Bragg angles are observed, suggesting subtle changes in the lattices. The lower intensities of the diffraction peaks of  $1 \cdot 2\text{H}_2\text{O}$  compared to those of  $2 \cdot 2\text{H}_2\text{O}$  are indicative of the low crystallinity of  $1 \cdot 2\text{H}_2\text{O}$ . Upon further heating to 500 K to give anhydrous forms of **1** and **2**, PXRD patterns exhibit different diffractions from those of the partially dehydrated forms, suggesting structural changes upon dehydration. Interestingly, whereas the partially dehydrated forms ( $1 \cdot 2\text{H}_2\text{O}$  and  $2 \cdot 2\text{H}_2\text{O}$ ) show similar PXRD patterns, PXRD patterns of the anhydrous forms **1** and **2** are different, indicating different structures. PXRD patterns measured at 550 K are similar to those at 500 K. These observations are consistent with the TG findings of a first dehydration step to form partially dehydrated samples, followed by a second step to form the anhydrous phases. After anhydrous phases **1** and **2** were cooled to room temperature and exposed to air for 1 week, PXRD measurements were performed. Bragg angles of **1** remain unchanged from that of the anhydrous phase over a period of 1 week. The anhydrous phase **1** appears to be stable in air. The anhydrous **1** could be converted back to the virgin  $1 \cdot 10\text{H}_2\text{O}$  by soaking in water for a sufficient amount of time, but showed somewhat low crystallinity (Figure 5d). On the other hand, with rehydration in air for **2**, the reverse process is observed. The PXRD pattern of the rehydrated form of **2** is almost identical to that of the virgin sample,  $2 \cdot 10\text{H}_2\text{O}$ , and the diffraction peaks sharpen considerably, indicating an increased long-range ordering of the structure.



**Figure 5.** Temperature-dependent PXRD patterns of  $1 \cdot 10\text{H}_2\text{O}$  (left) and  $2 \cdot 10\text{H}_2\text{O}$  (right): (a) room temperature, (b) 350 K, (c) 500 K, and (d) after soaking in water for 1 and exposed to air at room temperature for 1 week for **2**.

### 2.3. Reversible Dehydration-Rehydration and Structural Transformation

Figure 6 shows the results of water adsorption–desorption isotherm measurements for **1** and **2**, respectively. The samples were dehydrated at 493 K for 3 h to give the anhydrous forms before measurements, and water adsorption–desorption isotherm measurements were carried out at 298 K. The same measurements were performed using the same sample without further dehydration processes. For the anhydrous form, **1**, the adsorbed amount of water gradually increased with increasing pressure up to  $P/P_0 = 0.6$ , followed by an abrupt water uptake from  $P/P_0 = 0.6$ – $0.9$  (Figure 6 [1<sup>st</sup> (Co)]). The numbers of water molecules per molecular unit are 2 and 8, corresponding to the partially dehydrated form and the virgin sample of **1**, respectively. This result is in good agreement with the PXRD measurements. When the relative pressure was decreased, the amount of water gradually decreased. An abrupt decrease of the water molecules was observed at  $P/P_0 = 0.1$  and the number of the remaining water molecules per molecular unit was 4. Subsequently, a second adsorption measurement was performed using the same sample (Figure 6 [2<sup>nd</sup> (Co)]). The amount of water uptake increased gradually with small steps to  $P/P_0 = 0.7$  and reached a maximum at  $P/P_0 = 0.9$ . The number of water molecules per molecular unit was 10, corresponding to the virgin sample of  $1 \cdot 10\text{H}_2\text{O}$ , and the number of water molecules decreased with decreasing pressure. Again, the number of remaining water molecules per molecular unit was 4. This water adsorption–desorption process is reproducible, as shown in Figure 6 [3<sup>rd</sup> (Co)]. These results suggest that 6 water molecules are labile and can be removed at 298 K simply by decreasing the relative pressure, suggesting that uncoordinated water molecules are released first, and then coordinated water molecules are lost due to the higher stability of the coordination bonding to the metal ions. Thus, the release of the 6 water molecules gives a chain compound,  $1 \cdot 4\text{H}_2\text{O}$ ,  $\{[\text{Co}(\text{H}_2\text{O})_4(\text{pyz})][\text{Co}(\text{tdpd})_2(\text{pyz})]\}_n$ . Interestingly, the water isotherm at 298 K shows an irreversible water adsorption–desorption, from  $1 \cdot 2\text{H}_2\text{O}$  to  $1 \cdot 10\text{H}_2\text{O}$ , while PXRD measurements indicate a reversible transformation by heating and cooling with high humidity, suggesting higher stability of  $1 \cdot 4\text{H}_2\text{O}$  at 298 K. This means  $1 \cdot 4\text{H}_2\text{O}$  is metastable.

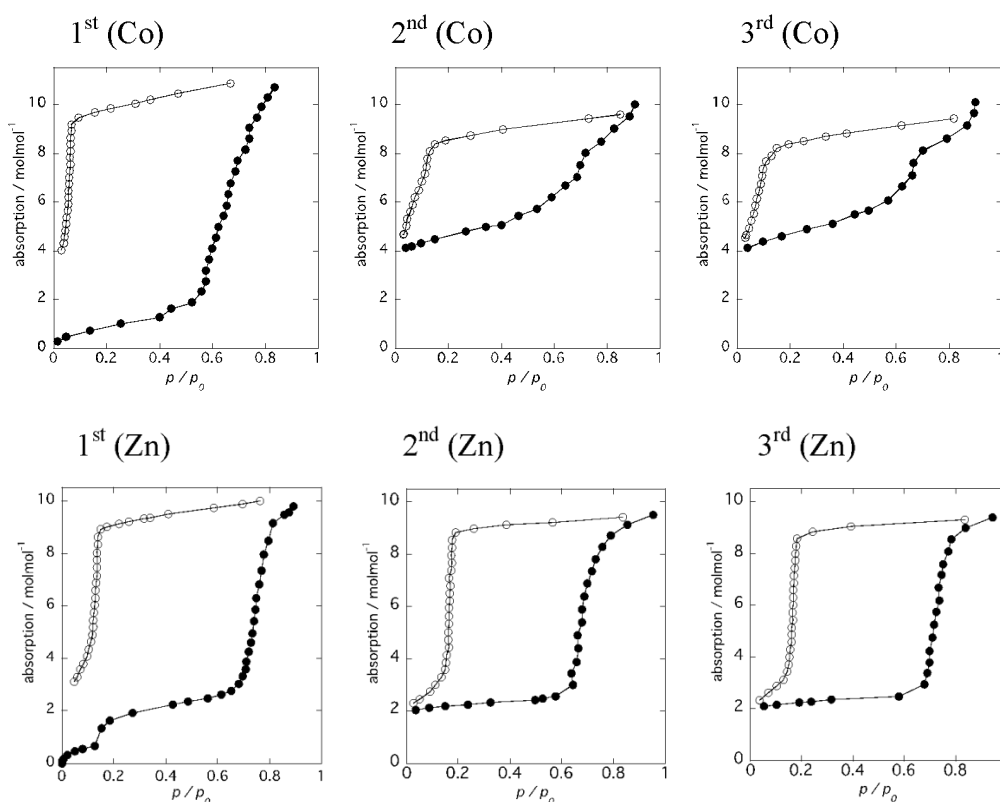
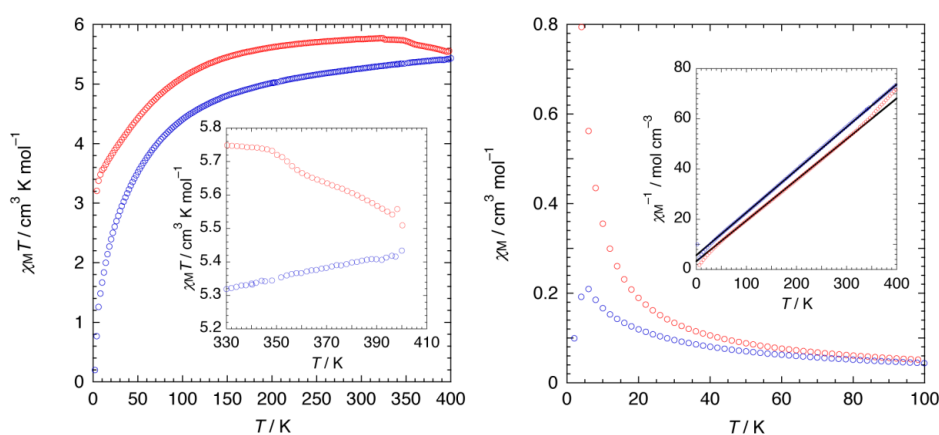


Figure 6. Results of water adsorption–desorption isotherm measurements for **1** (top) and **2** (bottom).

On the other hand, the water adsorption isotherm for the anhydrous form **2** displayed distinct steps at  $P/P_0 = 0.1$  and  $0.7$ , with a large hysteresis loop, as shown in Figure 6 [1<sup>st</sup> (Zn)]. The numbers of adsorbed water molecules were 2 and 8, respectively. These values are similar to those of anhydrous **1** and correspond to the partially dehydrated form,  $2 \cdot 2\text{H}_2\text{O}$ , and the hydrated form,  $2 \cdot 10\text{H}_2\text{O}$ , respectively. The pressure at the second step is higher than that of **1**, indicating the higher stability of the partially dehydrated form,  $2 \cdot 2\text{H}_2\text{O}$ . The desorption isotherm was similar to that of **1**; however, the number of remaining water molecules per molecular unit was 2, which is indicative of a structural transformation from the 1D chain compound,  $2 \cdot 10\text{H}_2\text{O}$ , to the 2D layer compound,  $2 \cdot 2\text{H}_2\text{O}$ . Subsequently, a second adsorption measurement was performed using the same sample (Figure 6 [2<sup>nd</sup> (Zn)]). The adsorption isotherm of  $2 \cdot 2\text{H}_2\text{O}$  exhibited an abrupt increase, and reached a plateau up to  $P/P_0 = 0.7$ , indicative of the structural stability of  $2 \cdot 2\text{H}_2\text{O}$ , while the adsorption isotherm of  $1 \cdot 4\text{H}_2\text{O}$  exhibited a gradual increase with increasing  $P/P_0$ . The number of water molecules decreased with decreasing pressure in the desorption isotherm. An abrupt decrease of the water molecules was observed at  $P/P_0 = 0.2$ . This water adsorption–desorption process was reproducible, as shown in Figure 6 [3<sup>rd</sup> (Zn)]. The large hysteresis of the adsorption–desorption curve is indicative of strong interactions between water molecules and zinc(II) ions.

#### 2.4. Magnetic Property

To further probe the structural change during the dehydration process, the magnetic susceptibility ( $\chi_M$ ) of  $1 \cdot 10\text{H}_2\text{O}$  was monitored in situ as a function of temperature, where the cobalt(II) ion in  $1 \cdot 10\text{H}_2\text{O}$  is paramagnetic. The temperature dependence of  $\chi_M$  of  $1 \cdot 10\text{H}_2\text{O}$  was measured over temperature ranges of 2–400 K (heating mode) and 400 K–2 K (cooling mode) in an applied field of 0.5 T (Figure 7). Upon heating, the  $\chi_M T$  value increased with increasing temperature, indicative of the existence of an antiferromagnetic interaction in the chains. A discontinuity of the  $\chi_M T$  value was observed around 350 K due to the loss of eight molecules of water, changing to a partially dehydrated form of  $1 \cdot 2\text{H}_2\text{O}$ . Plots of  $\chi_M^{-1}$  versus  $T$  were linear between 300 and 50 K for heating mode, and 400 and 50 K for cooling; Curie-Weiss fits ( $\chi_M = C/T - \theta$ ) for the data gave Curie constants ( $C$ ) of  $6.16$  and  $5.86 \text{ cm}^3 \text{ K mol}^{-1}$ . As the  $C$  values are higher than those predicted for a spin only value ( $C = 3.76 \text{ cm}^3 \text{ K mol}^{-1}$  with  $g = 2.00$ ), the strong magnetic anisotropy stemming from the unquenched orbital angular momentum must be invoked, whereas Weiss constants ( $\theta$ ) are  $-20.06$  and  $-33.23 \text{ K}$ , indicative of antiferromagnetic interactions between cobalt(II) centers. Interestingly, upon cooling, the magnetic behavior of  $1 \cdot 2\text{H}_2\text{O}$  is different from that of  $1 \cdot 10\text{H}_2\text{O}$ , suggesting the difference on the dimensionality of the compounds, as well as the coordination geometry.



**Figure 7.** Temperature dependence of DC magnetic data for  $1 \cdot 10\text{H}_2\text{O}$ . Red and blue open circles represent heating and cooling modes, respectively. (Left)  $\chi_M T$  versus  $T$  plot. Inset: An emphasized view of the high-temperature region. (Right)  $\chi_M$  versus  $T$  plot in the temperature region of 2–100 K. Inset:  $\chi_M^{-1}$  versus  $T$  plot with Curie-Weiss fits (solid black lines).

### 3. Experimental Section

#### 3.1. Materials and Methods

All chemicals were obtained from Tokyo Chemical Industry (TCI) Co., Ltd. (Tokyo, Japan), Wako Pure Chemical Industries, Ltd. (Osaka, Japan), and Sigma-Aldrich Japan (Tokyo, Japan), and used without further purification. Reactions and subsequent manipulations were performed under aerobic conditions at room temperature.

#### 3.2. Preparation of $\{[Co(H_2O)_4(pyz)][Co(tdpd)_2(pyz)] \cdot 6(H_2O)\}_n (1 \cdot 10H_2O)$

An aqueous solution of cobalt acetate dihydrate (20 mmol) and  $H_2tdpd$  (40 mmol) was transferred to a glass tube, then a methanol solution of  $pyz$  (40 mmol) was poured into the glass tube without mixing the two solutions. Orange crystals began to form at the ambient temperature in 1 week. One of these crystals was used for X-ray crystallography. Physical measurements were conducted on a polycrystalline powder that was synthesized as follows: An aqueous solution (30 mL) of cobalt acetate dihydrate (30 mmol) was added to an aqueous solution (30 mL) of  $H_2tdpd$  (60 mmol). After stirring the mixture, a methanol solution of  $pyz$  (60 mmol) was added. Upon stirring the mixture, orange powders were obtained. The powders were washed with water and methanol and dried in air (yield 70%). Calcd for  $1 \cdot 10H_2O$ :  $C_{20}N_{12}O_{14}H_{28}Co_2$ : C, 30.86; H, 3.63; N, 21.59. Found: C, 30.70; H, 3.52; N, 21.45. The identity of the batches for physical measurements and single-crystal data collection was established by comparison of the powder X-ray diffraction patterns. The experimental patterns of the powder samples were in good agreement with simulated patterns reproduced from the Fc values of the calculated crystal structures.

#### 3.3. Preparation of $\{[Zn(H_2O)_4(pyz)][Zn(tdpd)_2(pyz)] \cdot 6(H_2O)\}_n (2 \cdot 10H_2O)$ and Transformation to $[Zn_2(tdpd)_2(H_2O)_2(pyz)]_n (2 \cdot 2H_2O)$

An aqueous solution of zinc acetate dihydrate (20 mmol) and  $H_2tdpd$  (40 mmol) was transferred to a glass tube, then an ethanol solution of  $pyz$  (40 mmol) was poured into the glass tube without mixing the two solutions. Colorless crystals began to form at the ambient temperature in 1 week. One of these crystals was used for X-ray crystallography. Physical measurements were conducted on a polycrystalline powder that was synthesized as follows: An aqueous solution (30 mL) of zinc acetate dihydrate (30 mmol) was added to an aqueous solution (30 mL) of  $H_2tdpd$  (60 mmol). After stirring the mixture, a methanol solution of  $pyz$  (60 mmol) was added. Upon stirring the mixture, white powders were obtained. The powders were washed with water and methanol and dried in air (yield 70%). Calcd for  $2 \cdot 10H_2O$ :  $C_{20}N_{12}O_{14}H_{28}Zn_2$ : C, 30.36; H, 3.57; N, 21.24. Found: C, 30.60; H, 3.47; N, 21.35. The identities of the batches for physical measurements and single-crystal data collection were established by comparison of the powder X-ray diffraction patterns. The experimental patterns of the powder samples were in good agreement with simulated patterns reproduced from the Fc values of the calculated crystal structures.

The powders of  $2 \cdot 10H_2O$  were dried under reduced pressure ( $1.3 \times 10^{-1}$  Pa) at 350 K for 3 h, which were efficiently transformed to  $2 \cdot 2H_2O$ .

#### 3.4. Single-Crystal X-Ray Diffraction Measurement and Structure Determination

A suitable single-crystal was chosen and glued on the tip of a glass fiber. Diffraction data for complex  $1 \cdot 10H_2O$  and  $2 \cdot 10H_2O$  were collected on a Rigaku R-AXIS RAPID II IP diffractometer with a low-temperature apparatus (Rigaku Corporation, Tokyo, Japan) at 106 and 100 K, respectively. The diffractometer was equipped with graphite monochromated  $Mo-K\alpha$  ( $\lambda = 0.7107 \text{ \AA}$ ) radiation. The data were corrected for Lorentz and polarization effects. The structure was solved and refined using a combination of direct methods and Fourier techniques within the Rigaku CrystalClear crystallographic software package of Molecular Structure Corporation (Rigaku Corporation, Tokyo, Japan). The non-hydrogen atoms were refined anisotropically. The final

cycle of a full-matrix least-squares refinement was based on the number of observed reflections and variable parameters. No extinction corrections were applied. Details of the crystallographic data are given in Table 1 and cif files. The crystal data have been deposited at CCDC, Cambridge, UK and given the reference numbers CCDC1868638 and 1868639 for 1·10H<sub>2</sub>O and 2·10H<sub>2</sub>O, respectively.

### 3.5. Powder X-Ray Measurement and Structure Determination

The polycrystalline powder of 2·10H<sub>2</sub>O was initially placed in a borosilicate capillary and then was dried under a reduced pressure ( $1.3 \times 10^{-1}$  Pa) at 80 °C for 3 h to transform 2·2H<sub>2</sub>O. Powder diffraction data for the in-situ transformed 2·2H<sub>2</sub>O were collected on a Rigaku SmartLab automated multipurpose X-ray diffractometer (Rigaku Corporation, Tokyo, Japan) operating at 45kV/200 mA; 9 kW (Cu-K $\alpha$  radiation;  $\lambda = 1.5406$  Å) in the  $2\theta$  range of 5–90° with a scan speed of 0.5°/min at 298 K while continuously spinning. The reflection-intensity fitting and subsequent structure refinement using the Rietveld analysis were performed by the Rigaku software package PDXL (Rigaku Corporation, Tokyo, Japan).

### 3.6. Physical Measurements

Elemental analyses were performed on a J-Science Lab Micro Coder JM-11 (J-SCIENCE LAB Co., Ltd., Kyoto, Japan). Thermogravimetric analyses were performed on a Seiko Instruments TG/DTA6300 TG-DTA system (Seiko Instruments Inc., Chiba, Japan) under an N<sub>2</sub> atmosphere at a heating rate of 5 K/min. The water adsorption isotherm was measured using a BELSORP-max (MicrotracBEL Corp., Osaka, Japan) at room temperature after evacuating at 220 °C for 3 h. Magnetic measurements were made on a Quantum Design MPMS SQUID magnetometer (Quantum Design Japan, Inc., Tokyo, Japan) in the temperature range of 2–400 K and with an applied field of 5000 Oe. Temperature dependence X-ray diffraction patterns were carried out with a Rigaku SmartLab automated multipurpose X-ray diffractometer with a low-temperature apparatus (Rigaku Corporation, Tokyo, Japan) using Cu-K $\alpha$  radiation ( $\lambda = 1.5406$  Å).

## 4. Conclusions

In summary, two new 1D chain compounds have been identified in the reaction of M(II) (M = Co, Zn), H<sub>2</sub>tdpd, and pyz. The hydrogen-bonding assemblies obtained here reveal that the compounds consist of two types of 1D arrays. One is an anionic infinite pyz bridged 1D array, [M(tdpd)<sub>2</sub>(pyz)]<sup>2-</sup> (A), with chelating tdpd<sup>2-</sup> ligands, and the other is a cationic 1D array, [M(H<sub>2</sub>O)<sub>4</sub>(pyz)]<sup>2+</sup> (B), which is decorated with four terminal water molecules. The 1D arrays (A) and (B) are packed together by multi-point hydrogen-bonding interactions in an alternate (A)(B)(A)(B) sequence. Both compounds exhibit structural transformations, from a 1D chain structure to a 2D layer structure, driven by thermal dehydration processes at 350 K. The solid-state structural transformation from a 1D chain structure to a 2D layer structure, [Zn<sub>2</sub>(tdpd)<sub>2</sub>(H<sub>2</sub>O)<sub>2</sub>(pyz)]<sub>n</sub>, was revealed by X-ray structure analysis. Further heating to 500 K yielded anhydrous forms. While the virgin samples of cobalt(II) and (II) crystallized in different crystal systems, PXRD measurements of the dehydrated forms were indicative of the same crystal system. The transformation of the structure was irreversible for the cobalt(II) compound at the ambient condition. On the other hand, the zinc(II) compound showed a reversible structural change.

**Supplementary Materials:** The following are available online at <http://www.mdpi.com/2304-6740/6/4/115/s1>. Cif and cif-checked files. Figure S1: Rietveld refinement of PXRD pattern of 2·2H<sub>2</sub>O.

**Author Contributions:** R.I. and S.K. designed the project, summarized all the data provided by co-authors, and wrote the manuscript in consultation with S.Y. and H.K. S.Y., K.K., M.I., and H.K. synthesized all compounds and characterized them with elemental analyses. They also carried out thermogravimetric analyses, single-X-ray diffraction, variable-temperature powder X-ray diffraction, and water sorption-desorption measurements, respectively. H.K. carried out powder X-ray diffraction measurement of 2·2H<sub>2</sub>O and the Rietveld refinement using the diffraction data. S.H. performed the DC magnetic susceptibility measurement. All authors discussed the results and commented on the final version of the manuscript.

**Funding:** This work was supported by JSPS KAKENHI (Grant-in-Aid for Scientific Reserch (C), Coordination Asymmetry, Softcrystal); Grant Numbers 16K05735 and JP17H05390 (Satoshi Kawata), and 18H04529 (Ryuta Ishikawa). This work also supported in part by funds from the Central Research Institute of Fukuoka University; Grant Numbers 171011 (Satoshi Kawata) and 171041 (Ryuta Ishikawa).

**Conflicts of Interest:** The authors declare no conflicts of interest.

## References

1. Wu, W.-P.; Li, Z.-S.; Liu, B.; Liu, P.; Xi, Z.-P.; Wang, Y.-Y. Double-Step CO<sub>2</sub> Sorption and Guest-Induced Single-Crystal-to-Single-Crystal Transformation in a Flexible Porous Framework. *Dalton Trans.* **2015**, *44*, 10141–10145. [[CrossRef](#)] [[PubMed](#)]
2. Ling, S.; Slater, B. Unusually Large Band Gap Changes in Breathing Metal–Organic Framework Materials. *J. Phys. Chem. C* **2015**, *119*, 16667–16677. [[CrossRef](#)]
3. Han, J.; Nishihara, S.; Inoue, K.; Kurmoo, M. High Magnetic Hardness for the Canted Antiferromagnetic, Ferroelectric, and Ferroelastic Layered Perovskite-like (C<sub>2</sub>H<sub>5</sub>NH<sub>3</sub>)<sub>2</sub>[Fe<sup>II</sup>Cl<sub>4</sub>]. *Inorg. Chem.* **2015**, *54*, 2866–2874. [[CrossRef](#)] [[PubMed](#)]
4. Kataoka, S.; Banerjee, S.; Kawai, A.; Kamimura, Y.; Choi, J.-C.; Kodaira, T.; Sato, K.; Endo, A. Layered Hybrid Perovskites with Micropores Created by Alkylammonium Functional Silsesquioxane Interlayers. *J. Am. Chem. Soc.* **2015**, *137*, 4158–4163. [[CrossRef](#)] [[PubMed](#)]
5. DeCoste, J.B.; Peterson, G.W. Metal–Organic Frameworks for Air Purification of Toxic Chemicals. *Chem. Rev.* **2014**, *114*, 5695–5727. [[CrossRef](#)] [[PubMed](#)]
6. Karttunen, A.J.; Tynell, T.; Karppinen, M. Atomic-Level Structural and Electronic Properties of Hybrid Inorganic–Organic ZnO:Hydroquinone Superlattices Fabricated by ALD/MLD. *J. Phys. Chem. C* **2015**, *119*, 13105–13114. [[CrossRef](#)]
7. Sadakiyo, M.; Yamada, T.; Honda, K.; Matsui, H.; Kitagawa, H. Control of Crystalline Proton-Conducting Pathways by Water-Induced Transformations of Hydrogen-Bonding Networks in a Metal–Organic Framework. *J. Am. Chem. Soc.* **2014**, *136*, 7701–7707. [[CrossRef](#)] [[PubMed](#)]
8. Luo, L.; Zeng, Y.; Li, L.; Luo, Z.; Smirnova, T.I.; Maggard, P.A. Manganese–Vanadate Hybrids: Impact of Organic Ligands on Their Structures, Thermal Stabilities, Optical Properties, and Photocatalytic Activities. *Inorg. Chem.* **2015**, *54*, 7388–7401. [[CrossRef](#)] [[PubMed](#)]
9. Jiang, J.; Yaghi, O.M. Brønsted Acidity in Metal–Organic Frameworks. *Chem. Rev.* **2015**, *115*, 6966–6997. [[CrossRef](#)] [[PubMed](#)]
10. Oburn, S.M.; Bowling, N.P.; Bosch, E. Formation of Self-Complementary Halogen-Bonded Dimers. *Cryst. Growth Des.* **2015**, *15*, 1112–1118. [[CrossRef](#)]
11. Fan, H.; Shi, Q.; Yan, H.; Ji, S.; Dong, J.; Zhang, G. Simultaneous Spray Self-Assembly of Highly Loaded ZIF-8–PDMS Nanohybrid Membranes Exhibiting Exceptionally High Biobutanol-Permselective Pervaporation. *Angew. Chem. Int. Ed. Engl.* **2014**, *53*, 5578–5582. [[CrossRef](#)] [[PubMed](#)]
12. Yu, J.; Cui, Y.; Wu, C.-D.; Yang, Y.; Chen, B.; Qian, G. Two-Photon Responsive Metal–Organic Framework. *J. Am. Chem. Soc.* **2015**, *137*, 4026–4029. [[CrossRef](#)] [[PubMed](#)]
13. Podgajny, R.; Choraży, S.; Nitek, W.; Budziak, A.; Rams, M.; Gómez-García, C.J.; Oszajca, M.; Łasocha, W.; Sieklucka, B. Humidity-Driven Reversible Transformation and Guest Inclusion in a Two-Dimensional Coordination Framework Tailored by Organic Polyamine Cation. *Cryst. Growth Des.* **2011**, *11*, 3866–3876. [[CrossRef](#)]
14. Manna, B.; Desai, A.V.; Ghosh, S.K. Neutral N-Donor Ligand Based Flexible Metal–Organic Frameworks. *Dalton Trans.* **2016**, *45*, 4060–4072. [[CrossRef](#)] [[PubMed](#)]
15. Nagarkar, S.S.; Das, R.; Poddar, P.; Ghosh, S.K. Bistable Dynamic Coordination Polymer Showing Reversible Structural and Functional Transformations. *Inorg. Chem.* **2012**, *51*, 8317–8321. [[CrossRef](#)] [[PubMed](#)]
16. Couck, S.; Van Assche, T.R.C.; Liu, Y.-Y.; Baron, G.V.; Van Der Voort, P.; Denayer, J.F.M. Adsorption and Separation of Small Hydrocarbons on the Flexible, Vanadium-Containing MOF, COMOC-2. *Langmuir* **2015**, *31*, 5063–5070. [[CrossRef](#)] [[PubMed](#)]
17. Guerri, A.; Taddei, M.; Bataille, T.; Moneti, S.; Boulon, M.-E.; Sangregorio, C.; Costantino, F.; Ienco, A. Same Not the Same: Thermally Driven Transformation of Nickel Phosphinate-Bipyridine One-Dimensional Chains into Three-Dimensional Coordination Polymers. *Cryst. Growth Des.* **2018**, *18*, 2234–2242. [[CrossRef](#)]

18. Meng, X.-R.; Zhong, D.-C.; Jiang, L.; Li, H.-Y.; Lu, T.-B. Unprecedented Tuning of Structures and Gas Sorption Properties of Two 2D Nickel Metal–Organic Frameworks via Altering the Positions of Fluorine Atoms in Azamacrocyclic Ligands. *Cryst. Growth Des.* **2011**, *11*, 2020–2025. [[CrossRef](#)]
19. Douvali, A.; Tsiapis, A.C.; Eliseeva, S.V.; Petoud, S.; Papaefstathiou, G.S.; Malliakas, C.D.; Papadas, I.; Armatas, G.S.; Margiolaki, I.; Kanatzidis, M.G.; et al. Turn-On Luminescence Sensing and Real-Time Detection of Traces of Water in Organic Solvents by a Flexible Metal–Organic Framework. *Angew. Chem. Int. Ed. Engl.* **2015**, *54*, 1651–1656. [[CrossRef](#)] [[PubMed](#)]
20. Li, P.; Arman, H.D.; Wang, H.; Weng, L.; Alfooty, K.; Angawi, R.F.; Chen, B. Solvent Dependent Structures of Melamine: Porous or Nonporous? *Cryst. Growth Des.* **2015**, *15*, 1871–1875. [[CrossRef](#)]
21. Wang, H.; Li, B.; Wu, H.; Hu, T.-L.; Yao, Z.; Zhou, W.; Xiang, S.; Chen, B. A Flexible Microporous Hydrogen-Bonded Organic Framework for Gas Sorption and Separation. *J. Am. Chem. Soc.* **2015**, *137*, 9963–9970. [[CrossRef](#)] [[PubMed](#)]
22. Yamamura, Y.; Shimoi, H.; Sumita, M.; Yasuzuka, S.; Adachi, K.; Fuyuhiko, A.; Kawata, S.; Saito, K. Calorimetric Study of Correlated Disorder in [Hdamel]<sub>2</sub>[Cu<sup>II</sup>(tdpd)<sub>2</sub>·2THF Crystal. *J. Phys. Chem. A* **2008**, *112*, 4465–4469. [[CrossRef](#)] [[PubMed](#)]
23. Kawata, S.; Kumagai, H.; Adachi, K.; Kitagawa, S. Novel Layered Structures Constructed from Metal(II)–Chloranilate Monomer Compounds. *J. Chem. Soc. Dalton Trans.* **2000**, 2409–2417. [[CrossRef](#)]
24. Chuang, Y.-C.; Ho, W.-L.; Sheu, C.-F.; Lee, G.-H.; Wang, Y. Crystal Engineering from a 1D Chain to a 3D Coordination Polymer Accompanied by a Dramatic Change in Magnetic Properties. *Chem. Commun.* **2012**, *48*, 10769–10771. [[CrossRef](#)] [[PubMed](#)]
25. Adachi, K.; Sugiyama, Y.; Kumagai, H.; Inoue, K. Crystal Structures and Magnetic Properties of Novel Coordination Polymers with Rectangular Lattice Constructed from Pyrazine Derivative. *Polyhedron* **2001**, *20*, 1411–1415. [[CrossRef](#)]



© 2018 by the authors. Licensee MDPI, Basel, Switzerland. This article is an open access article distributed under the terms and conditions of the Creative Commons Attribution (CC BY) license (<http://creativecommons.org/licenses/by/4.0/>).